X-ray reflectance and infrared spectroscopy study of plasma enhanced atomic layer deposited Al_2O_3 and SiO_2

Elena Ostrovskaia

School of Electrical Engineering

Thesis submitted for examination for the degree of Master of Science in Technology.
Espoo 15.03.2017

Thesis supervisor:

Prof. Harri Lipsanen

Thesis advisor:

M.Sc. (Tech.) Perttu Sippola

Aalto University
School of Electrical
Engineering

Author: Elena Ostrovskaia

Title: X-ray reflectance and infrared spectroscopy study of plasma enhanced atomic layer deposited Al_2O_3 and SiO_2

In this thesis, Al_2O_3 and SiO_2 thin films produced by plasma enhanced atomic layer deposition were studied using X-ray reflectance (XRR) and attenuated total reflection Fourier transform infrared spectroscopy (ATR-FTIR). Structural characterization of thin films such as thickness, roughness and density was obtained with the XRR technique. Qualitative chemical constitution of the samples was studied with infrared spectra. The samples were deposited using different plasma powers at low temperature ALD. The characteristic difference between as-deposited vs. 400 °C annealed Al_2O_3 thin films were investigated. In case of SiO_2, the effect of plasma time and ALD cycle number to thin film properties were analyzed.

It was found that thickness does not show any dependence on plasma power, but density is increasing with plasma power for Al_2O_3, while for SiO_2 no apparent dependence was revealed. Analysis of roughness showed that it increases with plasma power for Al_2O_3 and thin SiO_2 samples, while for thicker SiO_2 samples it does not change significantly.

Analysis of ATR-FTIR spectra showed that there was no significant thin film composition dependence on the different plasma powers. ATR-FTIR results revealed that the structure of Al_2O_3 includes stretching and bending modes of Al-O bonds and also have sharp valley of Si-O bond due to the presence of native oxide between the Al_2O_3 thin film and Si substrate. SiO_2 infrared spectra comprises Si-O bending and stretching bands and also bands connected with the presence of O-H groups. Also detectable traces of CH_3 impurities was found, especially in case of thicker SiO_2 thin films.

On the basis of the performed analysis the dependence of SiO_2 and Al_2O_3 thin film density, roughness, thickness and molecular constitution on plasma parameters was reported.

Keywords: PEALD, XRR, FTIR, oxide thin films, Al_2O_3, SiO_2, O_2 plasma, chemical composition, density, rougness, structural analysis

Preface

The experimental work for this thesis was done between 2016-2017 in Aalto university. I had a chance to know and work with a large number of skillful and exceptionally intelligent people from School of Electrical Engineering and Department of Electronics and Nanoengineering whom I want to express my gratitude to.

First and foremost I wish to thank my supervisor, Professor Harri Lipsanen for giving me the opportunity to do my Master's Thesis in Nanoscience and Advanced Materials group. Working in Micronova laboratories has been a privilege. I am grateful to M.Sc. Perttu Sippola for invaluable guidance, patience and strong support in my work. I would like to express a big thank-you for their invaluable contribution to this work and also for creating the opportunity for me to start a career in Finland.

I want to express my gratitude for profound instructions and for helpful ideas to Sami Suihkonen and Jori Lemettinen with whom I started the measurements and who helped me with a practical part of this work.

Furthermore, I would like to thank M.Sc. Zhen Zhu for PEALD fabrication and preparation of the studied samples and his instructions about the experimental design of this work. Moreover, I wish show appreciation to Sami Kujala who looked through my thesis text and provided valuable comments and also for his help with Latex programm and for his support in technical part of work.

Finally, I am grateful to Aalto University professors for their everyday hard labour which give me the knowledge to complete this work.

"What we usually consider as impossible are simply engineering problems. . . there's no law of physics preventing them."
— Michio Kaku

Espoo, 15.03.2017

Elena Ostrovskaia

Contents

Abbreviations

ALD	Atomic Layer Deposition
ALE	Atomic Layer Epitaxy
ATR	Attenuated Total Reflectance
BTBAS	Bis(Tertiary-Butylamino)Silane
CVD	Chemical Vapour Deposition
FTIR	Fourier Transform Infrared Spectroscopy
GPC	Growth Per Cycle
ICP	Inductively Coupled Plasma
IR	Infrared
MOSFET	Metal-Oxide-Semiconductor Field Effect Transistor
MOVPE	Metalorganic Vapour Phase Epitaxy
PDS	Programmable Divergence Slit
PEALD	Plasma Enhanced Atomic Layer Deposition
PECVD	Plasma Enhanced Chemical Vapour Deposition
PEN	Polyethylene Naphthalate
REALD	Radical Enhanced Atomic Layer Deposition
TMA	Trimethylaluminium
XRD	X-ray Diffractometry
XRR	X-ray Reflectometry

1 Introduction

Nowadays, thin films are widely utilized as a part of wide range of applications and are under increasing research interest due to their wide and multi-functional properties. A thin film represents a layer of material with thickness ranging from fractions of a nanometer to several micrometers and today they are essential building blocks in electronics and semiconductor devices, LEDs, magnetic recording media, etc. In addition to the dimensional downscaling of technology, the reason for the widespread popularity of thin films is their often deviating material properties from the bulk materials. This difference can be very beneficial as it can be associated with eliminating unwanted effects, such as friction, current losses or reflection reduction or gaining positive properties such as surface hardening and strengthening. Moreover, they can work as diffusion, corrosion [1], moisture [2] or reflective [3] barriers. These benefits can be achieved especially well with metal oxide thin films, which have received significant amount of academic and commercial research interest during the digital era. Generally, metal oxides exist as solids at room temperature and they are typically inert in ambient condition.

The demand of conformality, uniformity and precise thickness control has made atomic layer deposition (ALD) one of the main techniques for sub-micrometer thin film deposition. ALD is a specialized chemical vapour deposition (CVD) method based on sequential pulses of two or more precursors that consecutively saturate the substrates surface and form a molecular compound layer with desired stoichiometry. [4] The significance of ALD is growing every year as the dimensions of devices are becoming smaller in size and their design is acquiring more complex and advanced properties from the thin films. ALD gives the opportunity for very uniform and conformal thin film deposition over large areas of complex geometries with accurate control of film thickness and excellent repeatability.

In addition to traditional thermal ALD, the metal oxide thin films can be produced

by subtype of ALD technique – plasma enhanced atomic layer deposition (PEALD). In PEALD of metal oxides, the oxidating precursor (typically oxygen) is only plasma activated since the growth behaviour of the plasma chemistry is more predictable than in case of more complex, metallic precursors. PEALD can be done in lower temperatures than the thermal ALD and thus enables wider variety of substrate and precursor materials.

The PEALD metal oxide thin films studied in this thesis are Al_2O_3 and SiO_2. These materials have traditionally been made by thermal ALD and the plasma parameters effect to the film properties are studied in this work because it is a new thing and can potentially widen the applicability of the materials. Al_2O_3 is an electrical insulator (with dielectric constant of 9.0 -10.1) with a relatively high thermal conductivity (ranging from 28-35 W/m-K) [5], it can be used in different applications such as protecting metal from oxidation and serving as an anti-corrosion coating. SiO_2 is one of the most important elements for microelectronics, it has high temperature stability, making it useful for process and device integration. Also it has very low refractive index which makes it lucrative for optical applications.

In this work, analysis of the structural and chemical properties of PEALD Al_2O_3 and SiO_2 thin films was made with X-ray reflectometry (XRR) and attenuated total reflection - Fourier transform infrared spectroscopy (ATR-FTIR) measurement equipment. The working principle of XRR lies in the reflection of X-rays from the differing electron densities of materials interfaces and detecting the angle dependent intensity. [6] With proper fitting algorithm, this method gives information about thin film density, thickness and roughness. FTIR is a technique that is used to obtain an infrared (IR) spectrum of absorption for study of chemical composition of materials. [7]

This thesis is structured as follows. Section 2 of this thesis covers the theoretical part, including ALD technique and its surface chemistry; different types of ALD,

XRR and FTIR measurement principles are discussed in this part as well. Section 3 describes the design of experiments consisting of the used ALD process parameters, measurement instrumentation and data handling models. Section 4 shows the analysis and results of the obtained data of ALD Al_2O_3 and SiO_2 thin film ATR-FTIR and XRR measurements. To conclude, the summary of the thesis is presented in Section 5.

2 Theoretical background

This section covers the ALD methods of thin films and different fabrication methods depending on reactor configurations. In addition, theory of two measurement techniques (XRR and FTIR) for finding characteristic data of thin films is discussed.

2.1 Atomic layer deposition

ALD is a special type of chemical vapour deposition (CVD) method where consecutively delivered source material gases or vapours produce thin films via self-saturative surface reactions. It is a very powerful technique that forms smooth thin films on versatile and complex substrate geometries allowing precise thickness and composition control. With a help of ALD, a wide range of materials can be produced such as conducting, insulating and semiconducting thin films in crystalline, poly crystalline and amorphous phases. They are usually inorganic binary compounds but can also be mono-, trinary- or higher order compounds. Using ALD it is possible to deposit various materials with an atomic-scale precision because ALD is based on sequential, self-limiting gas-solid reactions. [8] At least two gaseous reactants, called precursors, are involved in ALD process. They are sequentially introduced into the reactor with a separation step between them, called purge, during which all excess reactants and by-products are removed with inert gas flows. [4, 9]

A schematic representation of ALD process is shown in Figure 1, where reactants A and B are deposited separately on the substrate and the thin film is formed in four steps.
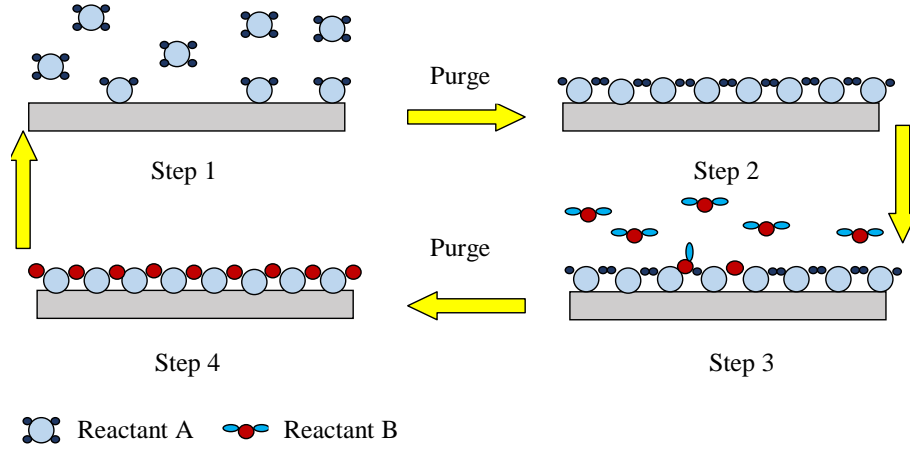
Step 1 Introducing precursor A and its self-limiting gas-solid reaction on the substrate surface.

Step 2 Purge for removal of gaseous reactants and by-products.

Step 3 Introducing precursor B and its self-limiting gas-solid reaction with the reactive

surface sites of A.

Step 4 Purge of un-reacted molecules and by-products. [11]

Figure 1. Illustration of typical two-component ALD process consisting of 4 steps. [10]

These steps form a reaction cycle and they can be freely repeated with constant material growth per cycle (GPC) resulting in desired film thickness. Because of the saturative surface growth, ALD process is self-limiting [12, 13], and when the maximum saturation level is reached the surface reactions terminate. The precursor dose can be adjusted with many different ways depending whether the precursor is in gas, solid or liquid phase on its initial form. One usual way to adjust the dose is to alter the pulse duration. A simplified representation of dependence between molecular surface coverage and pulse duration is shown in Figure 2, where upon reaching saturation step the amount of bonded reactant on the surface does not change anymore. Different three-dimensional geometries can be coated with material as topography only influences on the reaction components diffusion rate. [4, 14] Hence, thin film deposited by ALD can even coat trenched areas that are out-of-reach for other techniques if the precursor gas diffusion times are long enough.

One of the advantages of ALD process is the possibility of low deposition temperatures.
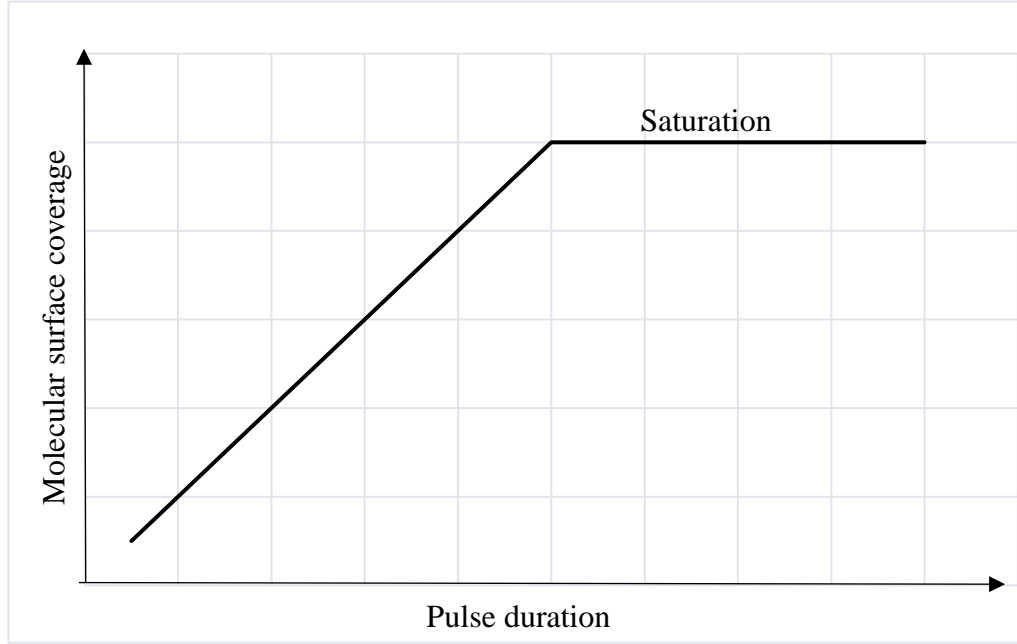
Figure 2. Schematic representation of precursor saturation.

The so-called ALD window describes the dependency of the growth rate on the deposition temperature where the GPC is nearly constant in the window and there are no parasitic reactions taking place. A generalized ALD window is represented in Figure 3 and its process specific range depends on the ALD chemistry in question. Therefore, the temperature for the ALD window can lay between 25-500 ℃.

The processes outside the ALD window cause non-saturative growth having too low or too high GPC's and poor film quality. At increased growth rate of thin films might cause precursor transfer from gaseous to liquid state, *i.e.*, condensate, at too low temperatures or decompose uncontrollably at too high temperatures. At too low temperature regime when the growth rate is low, the reactions can be incomplete due to insufficient reactivity. At too high temperatures and low growth rate the reaction can lead to precursor desorption. [12, 15] Thus, it is important to know at which temperatures the reactants saturate on the substrate surface. Choice of reactant pairs and materials that can be deposited is restricted because every material process has its individual ALD temperature window in which growth is saturated to a monolayer of film.
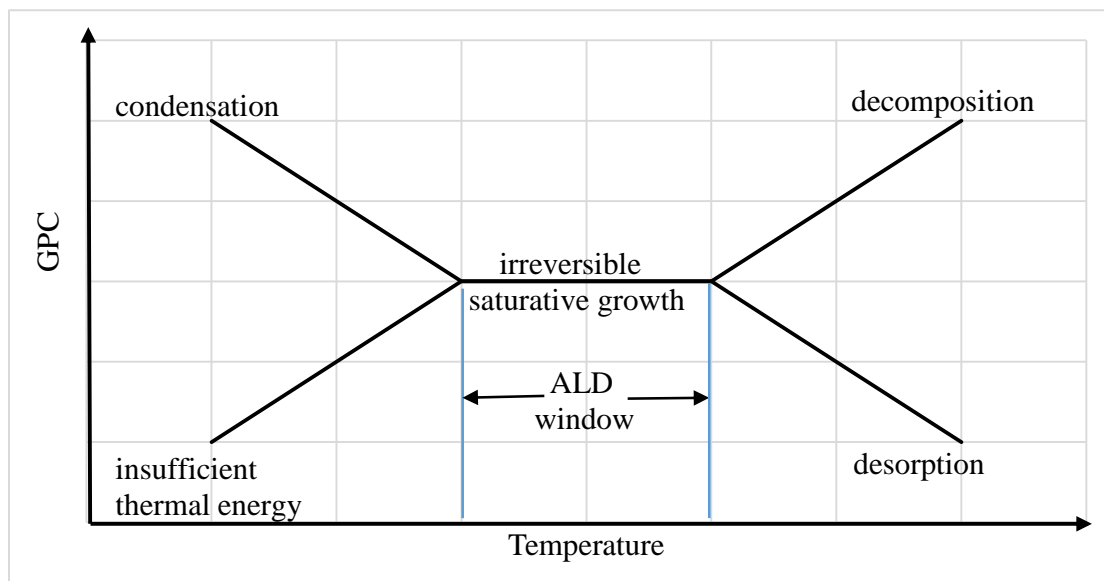
Figure 3. Schematic representation of a general ALD temperature window. ALD growth occurs within a temperature range determined by the reactants. [9]

It is noteworthy that the GPC can vary inside the ALD temperature window with changing substrate temperature, pressure or reactor geometry. In addition, the number of available reactive sites is influenced by the deposition temperature. Moreover, migration of above surface molecules of thin films can happen when the temperature is higher than ALD window temperature and even the direction of the chemical reaction mechanisms can be changed. [9]

2.1.1 Thermal and Plasma-Enhanced ALD

There are two reaction activation mechanisms used in ALD: thermal and plasma enhancement. Thus, ALD is usually divided into two subtypes: thermal ALD and PEALD. Only thermal energy is used to drive surface reactions in thermal ALD by supplying heat to the reaction chamber and thus to the substrate. However, there are several limitations for thermal ALD. First of all, the heating limitation of

ALD instruments is typically 500 ℃, thus, thermal energy is not always sufficient for complete reactions at reactor temperatures, which can cause incomplete growth or no growth at all. [15] Secondly, the choice of precursors is limited. PEALD increases variety of precursors and material selection as it can lower the deposition temperature to meet the low-temperature-reactive precursors and enables the increase of the deposition temperature to meet high-temperature-reactive precursors.

In PEALD, electrical or electro-magnetic energy is used to generate reactive species such as electrons, photons, ions and radicals of which only radicals are highly wanted in the process, others are tried to separate from the substrate. After acceleration and heating by electrical field or electro-magnetic field the radicals deliver a high, selective reactivity to surface without much thermal energy. Thus, PEALD allows more processing freedom including usage of a wider range of precursors. [17]

Depending on reactor design and interactions between plasma species and substrate, PEALD can be divided into radical enhanced, direct and remote plasma ALD. Different kinds of reactors for these specific PEALD types are presented in Figure 4. In direct PEALD, substrate is positioned as a part of or close to the plasma source and it can be involved in the generation of plasma species as a part of lower electrode, see Figure 4 (a). The close vicinity of plasma species might subject the substrate surface with ion bombardment, which can be harmful for delicate substrates and processes. The remote plasma ALD can be distinguished by the fact that the substrate is located remotely from the plasma source but close enough for mainly radicals to be present over the deposition surface with their quite low densities, Figure 4 (b). Moreover, the remote PEALDs usually apply inductively coupled plasma (ICP) generators which are responsible for locking the undesired charged particles around the coils magnetic field. In radical-enhanced ALD only radicals reach the surface as substrate is placed far from the plasma source, Figure 4 (c). The flux of radicals is significantly low because there are many collisions of

plasma species with each other and reactor walls. [9, 12, 17] Figure 4 (d) shows direct PEALD with mesh where the stage with the substrate works as a lower electrode and allows only radicals to enter the substrate space. [17] The analyzed samples were produced by this hybrid PEALD tool.
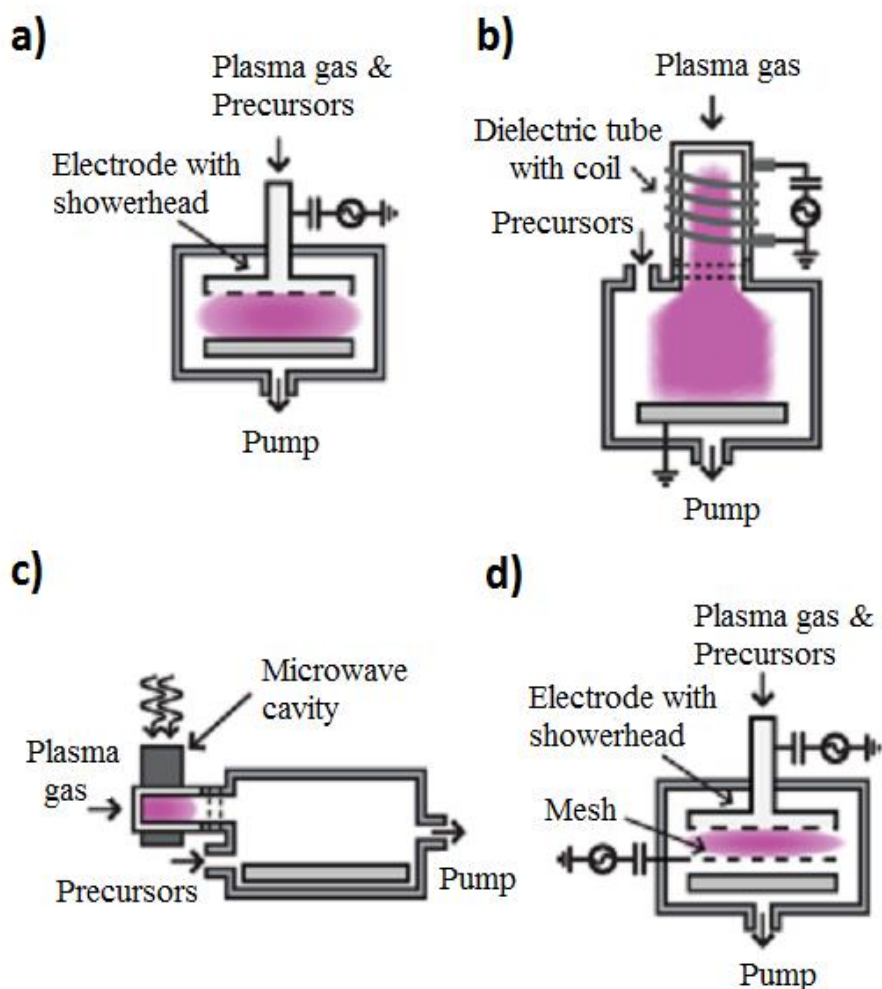
Figure 4. Schematic representation of various reactor configurations for PEALD: (a) direct PEALD, (b) remote PEALD, (c) radical-enhanced ALD, (d) direct PEALD with mesh. [17]

Although PEALD is more advantageous technique compared to thermal ALD due to more freedom of precursor choice, reduced substrate temperature and, in some cases, increased growth rate there are several challenges connected with it. Substrates with complex geometries are not covered as uniformly as lifetime of radicals tend to be low and their flow becomes more directional due to fast reaction on surfaces. Thus,

there might be not enough time for material deposition in deep trenches because of different collisions and because the lifetime of the radical can be shorter than the diffusion time into deep trenches. Moreover, high-energy species can cause damages of surface, including oxidation or nitridation of the top layer. [17]

2.2   X-ray reflectometry

X-ray reflectometry or X-ray reflectivity (XRR) is a surface-sensitive analytical technique used for structural thin film characterization. It measures the electron density profile based on $2\theta - \omega$ variations, which is used to derive information about thickness, density and interface roughness of thin films or multilayers at sub-nanometer scale using X-rays. [18] X-rays are electromagnetic waves of relatively high-energy photons with wavelength ranging from 0.01 to 10 nanometers.

The basic idea of the technique is to measure X-ray beam intensity reflected from the sample surfaces. The form of the reflected intensity as a function of the incident angle reveals information about the sample, where the measurement mode is $2\theta - \omega$ (2θ - angle between incident x-rays and detector, ω - angle between incident x-rays and sample surface). When incident beam reaches the sample at the greater angle than the angle of total reflection (*i.e.*, critical angle), part of incident beam penetrates into the material by transmission and drop in the reflected intensity occurs. In Figure 5 schematic view of X-rays reflections from thin film interfaces at the incident angle higher than the total reflection critical angle is shown.

The reflected wave experiences interference between material interfaces and creates intensity oscillation patterns (named as fringes) which are used to extract the structural data of a thin film. Thus, reflection pattern is seen as the X-ray intensity changes. [19, 20]

Another measuring mode of the X-ray diffractometer for the study of crystal structures and atomic spacing is XRD (X-ray diffraction). Interactions of these
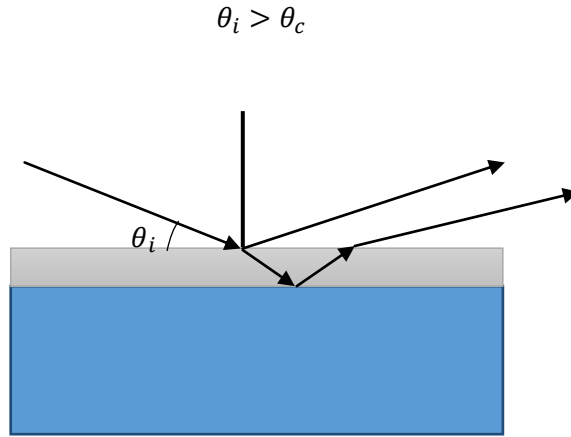
Figure 5. Interference of X-rays reflected from different interfaces at the incident angle higher than the total reflection critical angle. [18]

photons with the electrons of the material lead to diffraction of X-rays and produce a diffraction pattern, which contains information about the type and degree of crystallization in the substrate. X-ray diffraction takes place only at those particular angles of incidence, which satisfy the Bragg law. The law describes the wavelength of electromagnetic radiation in relation to the diffraction angle and the lattice spacing in a crystalline sample. [21]

$$n\lambda = 2d\sin\theta$$

where n - positive integer, λ - X-ray wavelength, d - spacing between planes of atoms.

For XRR and XRD measurements, sample surface should be uniform and homogeneous enough to reflect the beam without deviation.

In XRR method the reflectivity, oscillating frequency and amplitude are dependent on film thickness, density and roughness. Oscillating curves produced after the measurements can be analyzed by Fourier transform analysis, however as this method is not accurate enough, instead Parratt's formalism with curve fitting is commonly used. [22] Fitting can be performed by using genetic algorithms. It is a stochastic method based on the improvement of a population along successive generations. Each

generation is built from the parent generation by applying Parratt's formalism on the numbers of the parent generation.

The method has a number of advantages: different materials (conducting, insulating), structures (crystalline, amorphous) and sample sizes (even whole wafer) can be measured. It is also a non-destructive method as there is no physical contact with the sample during the measurement. However, the method requires predefined knowledge of the layer composition in order to determine thickness and density of layers later with proper modeling software.

2.3   Fourier transform infrared spectroscopy

Spectroscopy is a method for qualitative analysis of a sample based on interactions of electromagnetic radiation and matter. Absorption of electromagnetic radiation is dependent on the frequency of the radiation and the nature of the atoms in matter. When matter is exposed to IR radiation, atoms selectively absorb certain wavelengths that are characteristics of molecular structure. During the absorption, the vibrational energy levels experience transfer from ground state to excited state. [23, 24, 25] Only those vibrations that cause a dipole moment change, *i.e.*, the dipole moment must be different at the extremes of the vibration, are IR active. Molecules can vibrate in different vibrational modes, there are 5 main types of them. They are represented in Figure 6. However, it does not apply to all molecules, for instance, H_2 molecules can not be detected with FTIR. Besides non-symmetric, complex molecules could not have such modes. Thus, many vibrational modes can not be seen in FTIR spectra.

If vibration occurs as change in bond length then it is stretching, it can be symmetric, *i.e.*, stretching happens in the same direction, and asymmetric, *i.e.*, stretching happens in opposite directions. If vibration occurs as a change in bond angle, it is bending. Rocking vibration is where a group of atoms rotates part way
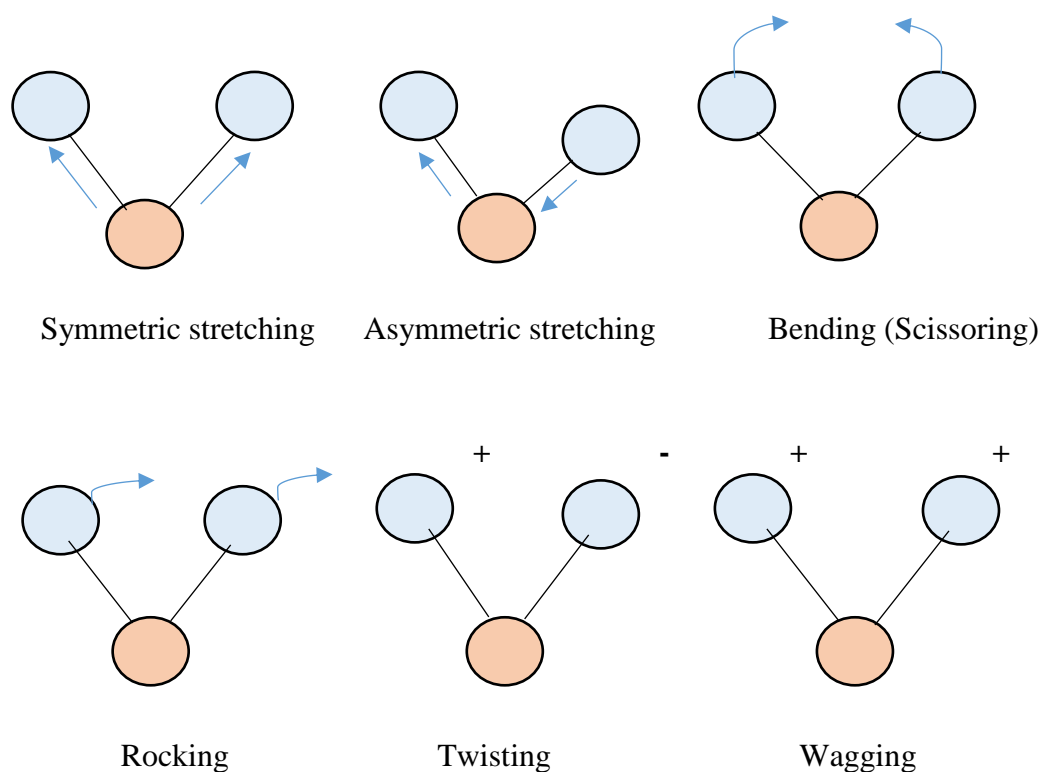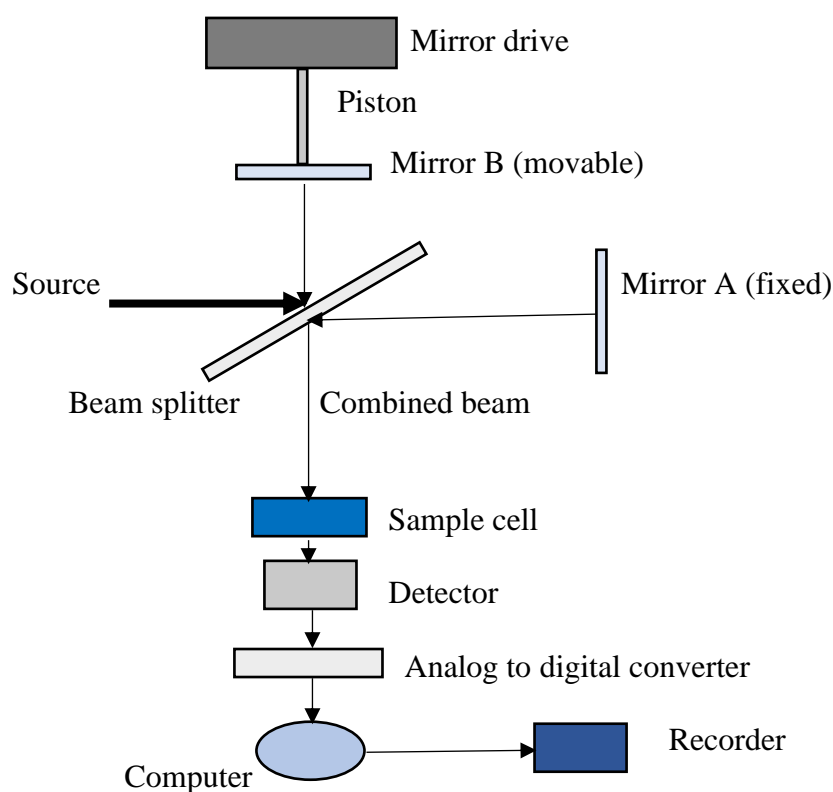
Figure 6. Schematic representation of molecular vibrations.

in one direction and part way in the other direction like a pendulum on a clock. Wagging vibration is a change in angle between a group of atoms. A change in the angle between the planes of two groups of atoms is called twisting. In rocking, wagging and twisting coordinate the bond lengths within the groups involved do not change. For FTIR spectroscopy the mid-IR region between 4000-400 cm^{-1} is used as most organic and inorganic compounds absorb within this region. [26]

If the investigated material consists of different molecules then its molecules have a large number of vibrational modes, thus, their spectra are very complex. Some vibrational modes can be attributed to individual functional groups. Molecular bonds of a sample can be qualitatively identified by analyzing wavenumber at the peak positions in an IR spectrum. Even though, IR spectrum does not provide quantitative data of molecular bonds, it gives information about functional groups, *i.e.*, groups of atoms in a compound that determine what kind of molecular bonds

are present in samples.

The working principle of FTIR spectrometer is based on interferometry and in most of them Michelson interferometer is used to split one beam of IR light into two. Then beams are recombined so that a path difference of two beams exists to produce interference. Schematic representation of an FTIR spectrometer is represented in Figure 7.


Figure 7. Schematic representation of a FTIR measurement system using Michelson interferometer configuration. [7]

Two mirrors and a beam splitter are the main components of Michelson interferometer, where one mirror is a stationary mirror and another is a movable mirror. The beam splitter transmits half of the light and reflects half of the incoming IR light. After passing the beam splitter, the transmitted light is directed to the stationary mirror while the reflected light is directed to the movable mirror. When the two beams are reflected back from the mirrors, they recombine with each other at the

beam splitter and constructive/destructive interference patterns are produced as a consequence of different distances covered by the two beams.

The sample is placed between the beam splitter and the detector, its selective absorption of the IR light causes changes in the intensity of energy reaching the detector. These fluctuations in the intensity produce an interferogram containing information about the IR spectrum of the sample; however this information is in the time domain. Fourier transformation, a mathematical algorithm that decodifies the interferogram, is used to transfer the interferogram from time domain to frequency domain. [7] After the Fourier transform, a plot of intensity of signal versus wavenumber is obtained.

Along with getting IR spectrum by transmitting the IR beam through the sample, reflectance of the sample can be used in an attenuated total reflectance (ATR) mode. In the ATR mode, incident IR beam propagates into the optically dense ATR crystal and experience the total internal reflection. This internal reflectance creates an evanescent wave that protrudes beyond the crystal surface and into the sample about 0.5-5 µm. Figure 8 shows the schematic representation of IR beam propagation in

Sample

Incident IR beam ATR crystal Attenuated IR beam
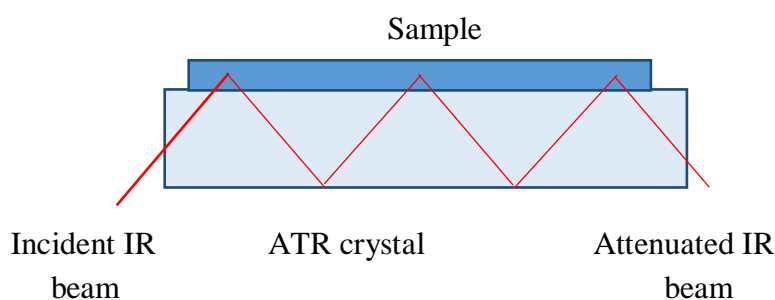
Figure 8. Schematic of IR beam propagation in ATR-crystal.

ATR-crystal. During the ATR measurements, the change in totally reflected IR beam, that happens when the beam is in contact with the sample, is detected. If the sample absorbs energy in some region, the evanescent wave will be attenuated or altered. The attenuated energy from each evanescent wave is passed back to the IR

beam, which then exits the opposite end of the crystal and is passed to the detector.
[27]

3 Research materials and methods

This section provides a review of PEALD process parameters for Al$_2$O$_3$ and SiO$_2$ that was studied in this thesis. This is followed by description of measurements and set-up of the used measurement methods. This section ends with discussion of data handling models of the measurement methods.

3.1 PEALD process parameters

3.1.1 Al$_2$O$_3$

The deposition of Al$_2$O$_3$ thin films was performed on n-type Si wafer with a thickness of 650 µm and orientation of (100) produced by Czochralski method. As a part of the experiments, Al$_2$O$_3$ was deposited with two types of ALD method - thermal and plasma-enhanced ALD with Beneq TFS-200 ALD-reactor. In the ALD-reactor "hybrid" plasma set-up was used where the plasma system was capacitively coupled with RF-power plasma system and the substrate was placed below the lower electrode of the reactor. For PEALD samples temperature of 90 ℃ and plasma powers of 50-300 W were utilized. Trimethylaluminium (TMA) served as Al precursor with 0.2 s pulse and 3 s purge times while O$_2$ plasma was used with 1-6 s pulse and 2 s purge times. One reference sample was produced with thermal TMA/H$_2$O ALD process at temperature of 150 ℃ referred as a reference sample. N$_2$ served as a carrier gas having a through-reactor flow of 300-600 sccm. Amount of ALD cycles was 200 for all samples. The operative pressure in the reactor was around 0.75 mbar.

After the deposition four samples were annealed, while five samples were left as-deposited, *i.e.*, without annealing. Al$_2$O$_3$ thin films annealing was implemented at 400 ℃ in N$_2$ atmosphere with rapid thermal annealing furnace for 30 min. ALD parameters of as-deposited and annealed Al$_2$O$_3$ samples are listed in Table 1 and Table 2, respectively. The following abbreviations are used to distinguish samples:

AO stands for as-deposited Al_2O_3 samples, while AOA for annealed Al_2O_3 samples, the number following after the abbreviation tells about power that was used to produce the samples.

Table 1. Main ALD parameters of as-deposited Al_2O_3.

Sample identifier	Power, W	Pulse, s	Temperature,℃	ALD method
AO T Ref			150	thermal
AO 50 W	50	1	90	plasma enhanced
AO 100 W	100	1	90	plasma enhanced
AO 180 W	180	1	90	plasma enhanced
AO 300 W	300	1	90	plasma enhanced

Table 2. Main ALD parameters of annealed Al_2O_3.

Sample identifier	Power, W	Pulse, s	Temperature, ℃	ALD mode
AOA T Ref			150	thermal
AOA 50 W	50	1	90	plasma enhanced
AOA 100 W	100	1	90	plasma enhanced
AOA 180 W	180	1	90	plasma enhanced

3.1.2 SiO_2

SiO_2 was deposited with PEALD method. PEALD parameters of SiO_2 samples are listed in Table 3. O_2 plasma served as an oxidizing agent with flow rate of 75 sccm. In the reactor plasma powers of 50-300 W with pulses of 1-6 s were utilized in order to study their effect to the structural and chemical thin film properties. After O_2 plasma pulse, 2 s purge time was applied and followed by bis(tertiary-butylamino)silane (BTBAS) precursor pulse with 0.3 s duration and consecutive 3 s purge time. N_2 was used as a carrier gas having a through-reactor flow of 800 sccm. During the deposition, the pressure in the reactor was around 1 kPa and 300 or 1000 PEALD cycles were performed to study thickness effect on the intended measurements. In Table 3, the sample identifiers comprises the information about number of cycles: SO1 and SO3 correspond to SiO_2 produced with 1000 number of cycles and to SiO_2

produced with 300 number of cycles, respectively. The second number that is used in the abbreviation is the length of plasma pulse and the third number is power.

Table 3. Main PEALD parameters of SiO_2.

Sample identifier	Number of cycles	Power, W	Plasma pulse, s
SO1 1 s 50 W	1000	50	1
SO1 1 s 180 W	1000	180	1
SO1 3 s 180 W	1000	180	3
SO1 6 s 180 W	1000	180	6
SO1 1 s 300 W	1000	300	1
SO3 1 s 50 W	300	50	1
SO3 1 s 180 W	300	180	1
SO3 3 s 180 W	300	180	3
SO3 6 s 180 W	300	180	6
SO3 1 s 300 W	300	300	1

## 3.2 Measurements and set-up

3.2.1 XRR

X-ray reflectivity measurements were carried out with a Philips X'Pert Pro instrument. The set-up with appropriate X-ray optics and accessories that was used in the experiments is shown in Figure 9. X-ray tube consists of an evacuated envelope with an anode, a cathode, a focusing cylinder and exit window. A current that is passed through the cathode creates thermal emission of electrons. Because of high voltage difference between the anode and the cathode, the electrons are accelerated toward the anode. At the maximum voltage of 60 kV the electrons striking the anode that is made of Cu cause emission of X-rays with wavelength of 0.15 nm. These X-rays leaves the tube through the exit window.

Upon exiting the window, X-ray beam passes through 1/2 ° divergence slit that is used to control the divergence of the incident X-ray beam, and thus the irradiated length on the sample. If divergence slits are used with a combination of an X-ray

mirror, they control the height of the emerging X-ray beam rather than the divergence. After the divergence slit, the beam is directed to Cu attenuator where its intensity reduction occurs. The parabolic X-ray mirror converts the divergent X-ray beam from the X-ray tube to an monochromatic quasi-parallel beam. Programmable divergence slit (PDS) is used for low angle measurements as reflectivity applications. Soller slits control the axial divergence of the X-ray beam. Mask is used to control the irradiated width on the sample.

Then the beam is directed to the sample on which it reflects to the collimator. The collimator causes the direction of reflected beams become more alinged in the propagation direction and only beams that are traveling parallel exit the collimator. Before entering the detector, where the intensity of the diffracted beam is counted, the beam passes monochromator to filter undesired wavelengths. The X-ray detector is the last item on the X-ray beam path. The detector consists of a transducer and a pulse forming circuit. The transducer collects and converts the incoming X-ray photons to electric current. The pulse forming circuit converts this current into electrical pulses which are counted by the electronics for further processing. The detector is most effective for Cu radiation with efficiency of 84 %. [28]
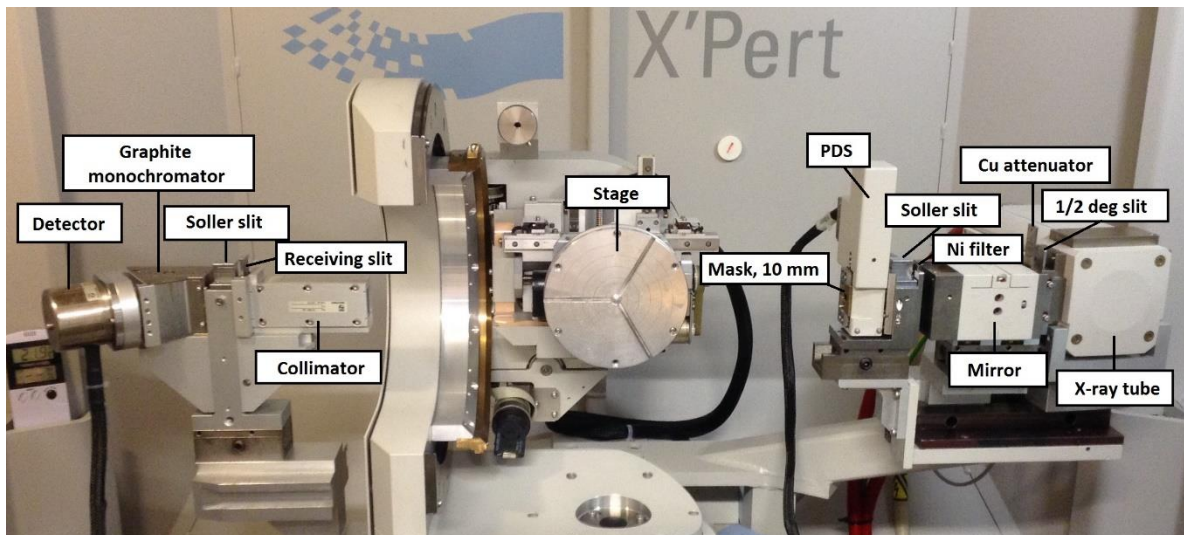
Figure 9. Used optic elements in the X-ray reflectivity measurement set-up.

The alignment procedure should be done before the actual measurements, where

it is ensured that a sample and a detector are aligned with the X-ray beam. The procedure is shown in Figure 10 and contains the following steps:

Step 1 X-ray beam maximum intensity is measured. On the stage there is no sample that blocks the beam, and 2θ angle (*i.e.*, twice the reflection angle, which is also ω angle) is scanned around the default zero point. If the found maximum beam intensity is at a slightly different angle, then it is set as the new zero point for the measurements, Figure 10 (a).

Step 2 A sample is attached to the stage with a tape and moved in z-direction in the position where it partly blocks the beam. The point where the intensity drops to half from its maximum value is found with monitoring the number of counts, Figure 10 (b). This step insures that the incident beam illuminates the sample.

Step 3 The ω angle is then scanned around the "new zero" point found in the step 1 in order to set the sample surface to be accurately parallel with the beam, Figure 10 (c). If the maximum value is observed at an angle slightly different from the initial angle then adjustment is done in order to avoid misalignment of the sample and the beam. The sample position is tuned again to block approximately half of the beam, followed by another ω scan.

Step 4 The parallelism of the sample and the beam is confirmed by setting the angles ω and 2θ to values 0.2 ° and 0.4 °, respectively, and the ω angle is scanned across narrow angle range. Since 0.2 ° is smaller than the critical angle of total reflection for samples, a narrow and intense peak is observed at an angle, with which the condition for total reflection (*i.e.*, $\omega = \theta$) was fulfilled, Figure 10 (d).

After these calibration steps, the obtained values corresponding the maximum intensity are set to be the new zero values for the actual measurements.

The actual measurements were performed in 2θ-ω mode, *i.e.*, the angles between
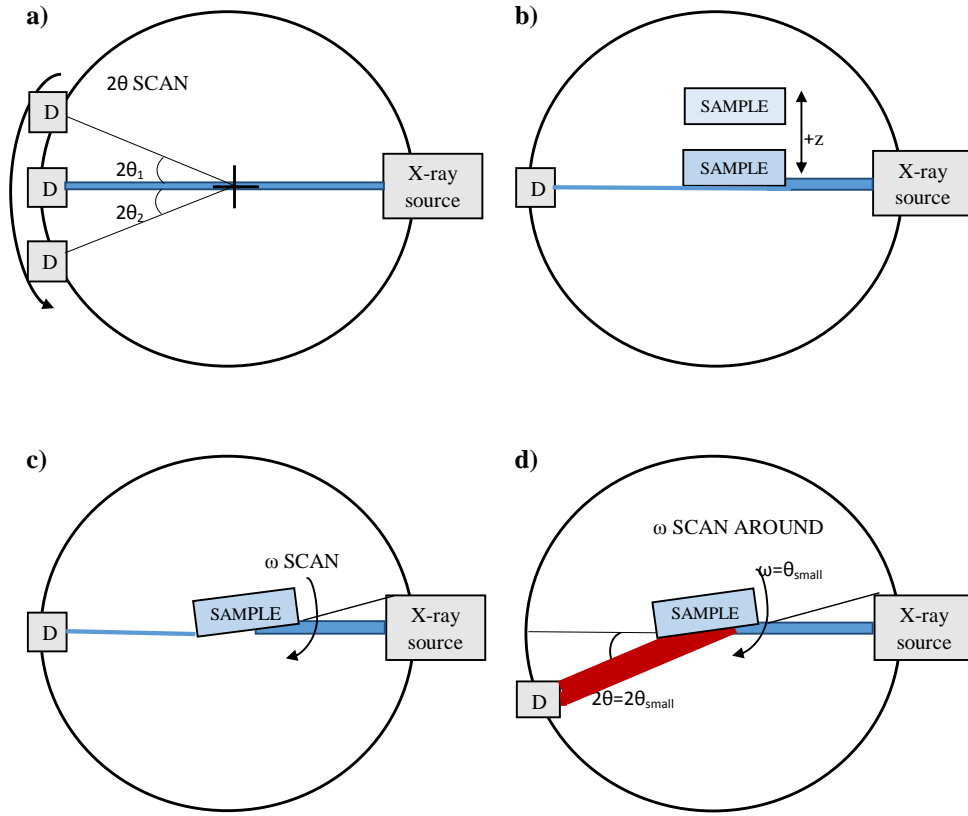
Figure 10. Alignment procedure for XRR set-up.

the sample surface and the incident and reflected beam were kept equal, while the angle ω was scanned. The ω scan range was 0.1 ° - 3.0 °. This range was chosen in order to be able to observe the maximum reflected intensity and oscillations due to interference phenomenon. Also the sampling parameters of the scans were chosen to provide high resolution. However, the measurement time was kept in reasonable limits, and the full continuous scan in the chosen angle range took approximately 24 minutes for one sample.

3.2.2   FTIR

IR spectra were obtained using Nicolet Magna 380 FTIR spectrometer. There are two possible measurement modes: transmission and ATR. The samples were

measured with ATR mode where the sample reflectance was used. ATR-FTIR set-up is shown in Figure 11. The optically dense crystal with high refractive index, *i.e.*, ATR crystal, was a diamond. ATR crystal, on which the sample is placed for measurements, is situated in the middle of a stage.
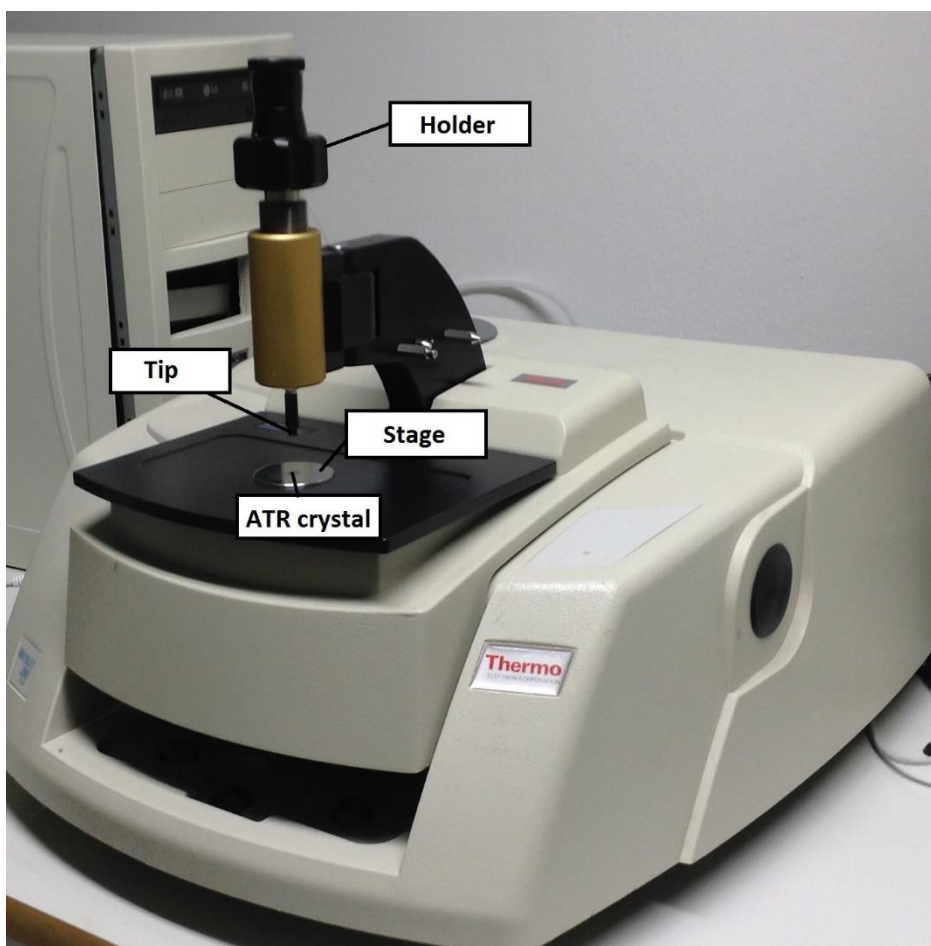
Figure 11. Set-up for IR spectrum measurement in ATR-FTIR mode.

The environment in which the sample is placed has traces of gases and molecules. These molecules and gases being not the sample itself contribute to measured data of the sample, therefore, FTIR measurements require collecting a background spectrum before actual measurements. The background spectrum contains information about the species of gases and solvent molecules, such as ambient water and carbon dioxide, which may then be subtracted away from sample spectrum in order to get only sample information. The background spectrum also takes into account spectrum

artifacts related to the instrument performance such as information about the source, interferometer and detector.

After the background collection, a sample is placed on the stage with the ATR crystal in the middle and fixed with a tip by screwing a holder handle. The tip that presses the sample to ATR crystal ensures good contact between them. It is necessary due to the small extension of the evanescent wave beyond the crystal and to achieve high quality results. The IR beam enters ATR crystal from the bottom, extends in the sample and upon exiting the crystal it is directed to the detector. OMNIC software is used to collected sample spectrum. The spectrum of sample is the subtraction of sample spectrum and background spectrum. The sampling parameters were chosen to get high quality spectra thus the number of scans was increased to 300.

3.3 Data handling models

3.3.1 XRR

XRR raw data is usually represented and handled as a graph with normalized logarithmic intensity y-axis and linear 2θ-ω x-axis. A logarithmic scale is used because of the wide dynamic range of X-ray reflectivity intensity. The fitting of theoretical model was done on top of the measured plot with in-house XRR fitting software, where the simulated plot is fitted to the measured plot using genetic algorithm. [22] In Figure 12 there is an example of the measured plot of as-deposited Al_2O_3 sample AO 180 W fit with a theoretical plot. To create a layer model it is necessary to enter approximate values of density, roughness and thickness of substrate and thin films. Densities can be found if the thin film and the substrate materials are known. Thicknesses of thin films are usually proportional to the number of deposition cycles, and its approximate value can be found. Minimum and maximum limits for the data should be also defined in the program so it is possible to use automatic and manual

fitting modes. The solution with optimal parameter values of thickness, density
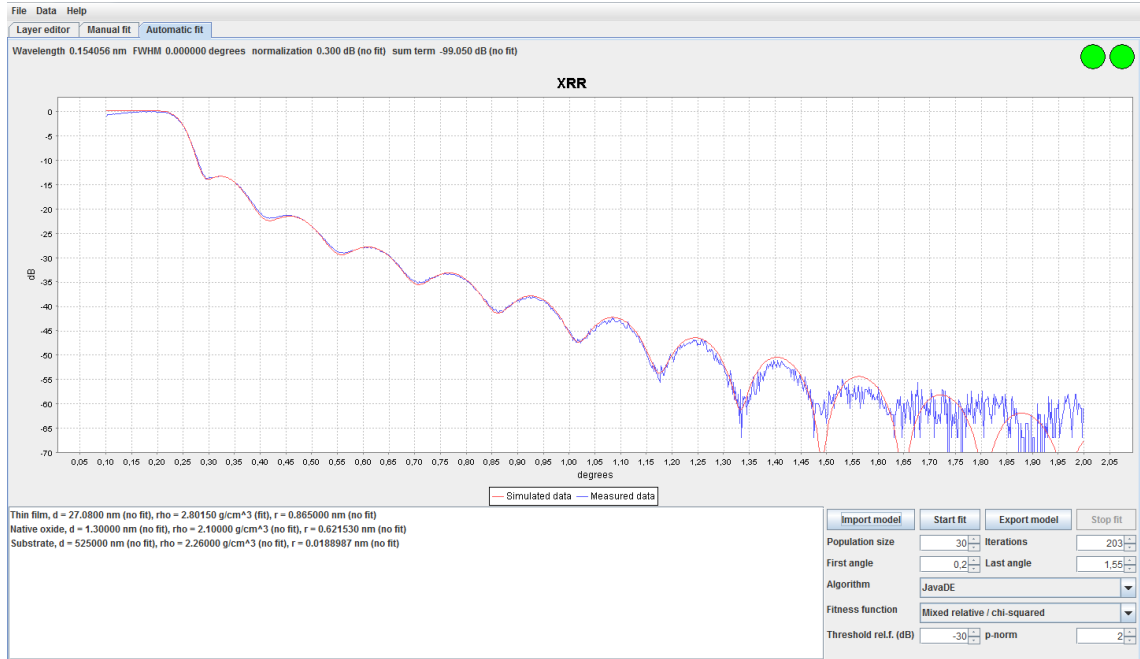
Figure 12. Example of good fitting, sample: as-deposited Al_2O_3 produced at 180 W plasma power PEALD, AO 180 W. The blue curve represents a measured sample data, the red curve is a theoretical curve fitted on top of the measured one. The found data of thickness, roughness and density of the structure is displayed in the left corner in the programm.

and roughness of the interface of multilayer film is obtained when the difference between the measured and theoretical reflectivity data reaches a minimum. The model frequency, wavelength, amplitude and decay trend hold the information about the film thickness, density and roughness. On the graphs, the reflectivity profiles show oscillations caused by X-ray interference of reflected beams from the interfaces of the sample. The wavelength depends on film thickness and the period of oscillations becomes shorter if the film thickness is increasing. The amplitude of the oscillation and the exact location of the critical angle provide information on the density of film, which means that the larger the thin film density the higher the amplitude of the oscillations. If the surface roughness is large, the reflected X-rays decrease more rapidly. In addition, the amplitude of the oscillation decreases with increasing interface roughness.

To derive the structural information from the reflectivity oscillations of the raw data in fitting programm, it was more effective to use automatic and manual fitting together. First preliminary fitting was done with automatic mode where the programm finds the best suitable parameters. However, they were not always the best match, thus it was necessary to use manual mode where parameters were defined by a programm user. This mode gave better results but also finding the most suitable fit was time consuming. [29]

3.3.2 ATR-FTIR

The measured ATR-FTIR spectra are represented in a form of transmitted or absorbed intensity versus wavenumbers. Wavenumbers are in x-axis in units of inverse centimeters, intensities are plotted in y-axis in percentage units, which are provided by the FTIR software. Figure 13 shows the raw data graph after ATR-FTIR measurement of SiO_2 SO1 1 s 300 W.

Data analysis consists of several steps. Firstly, the characteristic valleys are determined in the IR spectrum. Then those valleys are compared with reference FTIR database or earlier published FTIR analysis articles about the same materials. In the end, the absorption wavenumber bands in the sample spectrum are assigned to the most probable molecular vibration modes. After the analysis, the molecular structure is qualitatively linked to the observed spectrum.
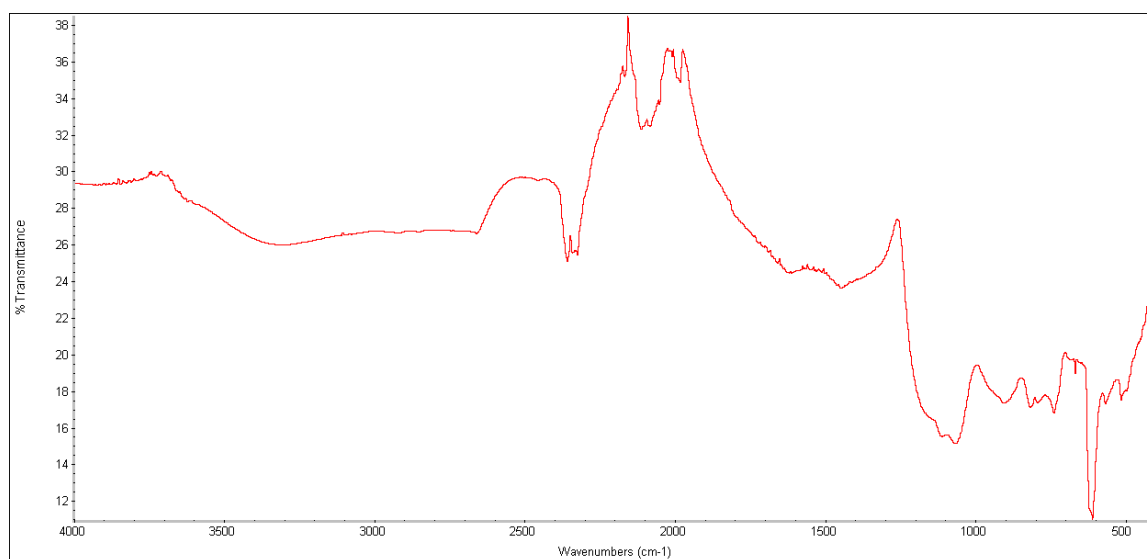
Figure 13. Example of ATR-FTIR graph, sample: SiO_2 produced with 1000 ALD cycles at 300 W plasma power and 1 s plasma pulse, SO1 1 s 300 W. Valleys represent characteristic molecular vibrations.

4   Results

This section focuses on the results and contains two parts, the first part discusses the results obtained using XRR method, while the second part comprises ATR-FTIR measurement results for Al_2O_3 and SiO_2 samples.

4.1   XRR measurement results

This section is divided into two subsections, the first one covers the XRR results of Al_2O_3 and the second one those of SiO_2. Thickness, density and roughness of the thin films were found utilizing in-house XRR fitting software.

4.1.1 Al_2O_3

The dependency of process parameters of plasma power and annealing were studied with respect to the structural thin film properties of density, roughness and thickness. According to results, plasma power and annealing treatment influence to Al_2O_3 thin film properties was observed. If plasma power is low thus it activates the precursor gases partially and can lead to incomplete surface reaction. In case of the annealing effect to low-temperature, amorphous thin films can experience roughness improvement and surface smoothing [30], moreover, it can reduce stress and strain. The AOA samples were subjected to low-temperature annealing treatment which purpose was not crystallization of the thin films but to see annealing effect to structural properties of amorphous Al_2O_3 thin film. On the contrary, high temperature annealing leads to thin film crystallization and as a consequence increases roughness.

The XRR measurements fitting results such as thickness, density and roughness of as-deposited and annealed Al_2O_3 samples at temperature of 400 ℃ are listed in Table 4 and 5, respectively. The process of finding the best fit for Al_2O_3 XRR data was challenging due to a presence of native oxide with average thickness of 1.2 nm for the as-deposited and 1.9 nm for the annealed samples in between of Al_2O_3

and Si substrate. Thus, the observed structure was Si-SiO_2-Al_2O_3. The fitting has error margins such as 0.12 nm for thickness, 0.11 g/cm^3 for density and 0.06 nm for roughness according to the formalized error that gives an asymptotic estimate and provides reasonable corrections in the case of systematic error caused by nonideal fit. [31]

Table 4. XRR fitting results of as-deposited Al_2O_3.

Sample identifier	Thickness, nm	Density, g/cm^3	Roughness, nm
AO T Ref	25.90	3.16	0.54
AO 50 W	27.40	2.65	1.28
AO 100 W	26.20	2.85	0.67
AO 180 W	27.10	2.80	0.87
AO 300 W	39.90	2.82	0.75

Table 5. XRR fitting results of annealed Al_2O_3.

Sample identifier	Thickness, nm	Density, g/cm^3	Roughness, nm
AOA T Ref	25.40	2.88	0.38
AOA 50 W	26.20	2.62	0.15
AOA 100 W	25.90	2.67	0.39
AOA 180 W	26.50	2.78	0.47

In Figure 14, density, roughness and thickness dependence of plasma power to annealed and as-deposited Al_2O_3 is represented. According to the found results for density, Figure 14 (a), dependence of the annealed and the as-deposited samples differ from each other at 100 W plasma power and are practically the same at 50 W and 180 W. The annealed sample densities undergo decrease of 0.05 g/cm^3 from 50-100 W plasma power while the as-deposited sample density experience increase of 0.20 g/cm^3 in the same plasma power interval. This result shows deviation from the trend which can be caused by non-ideal fitting of Al_2O_3 annealed samples. Density increase or decrease of 0.11 g/cm^3 can be considered as error margins caused by a non-ideal measurement and fit in the fitting programm. [31] Thus, such fluctuation as 0.05 g/cm^3 can be neglected. Including error margins the overall
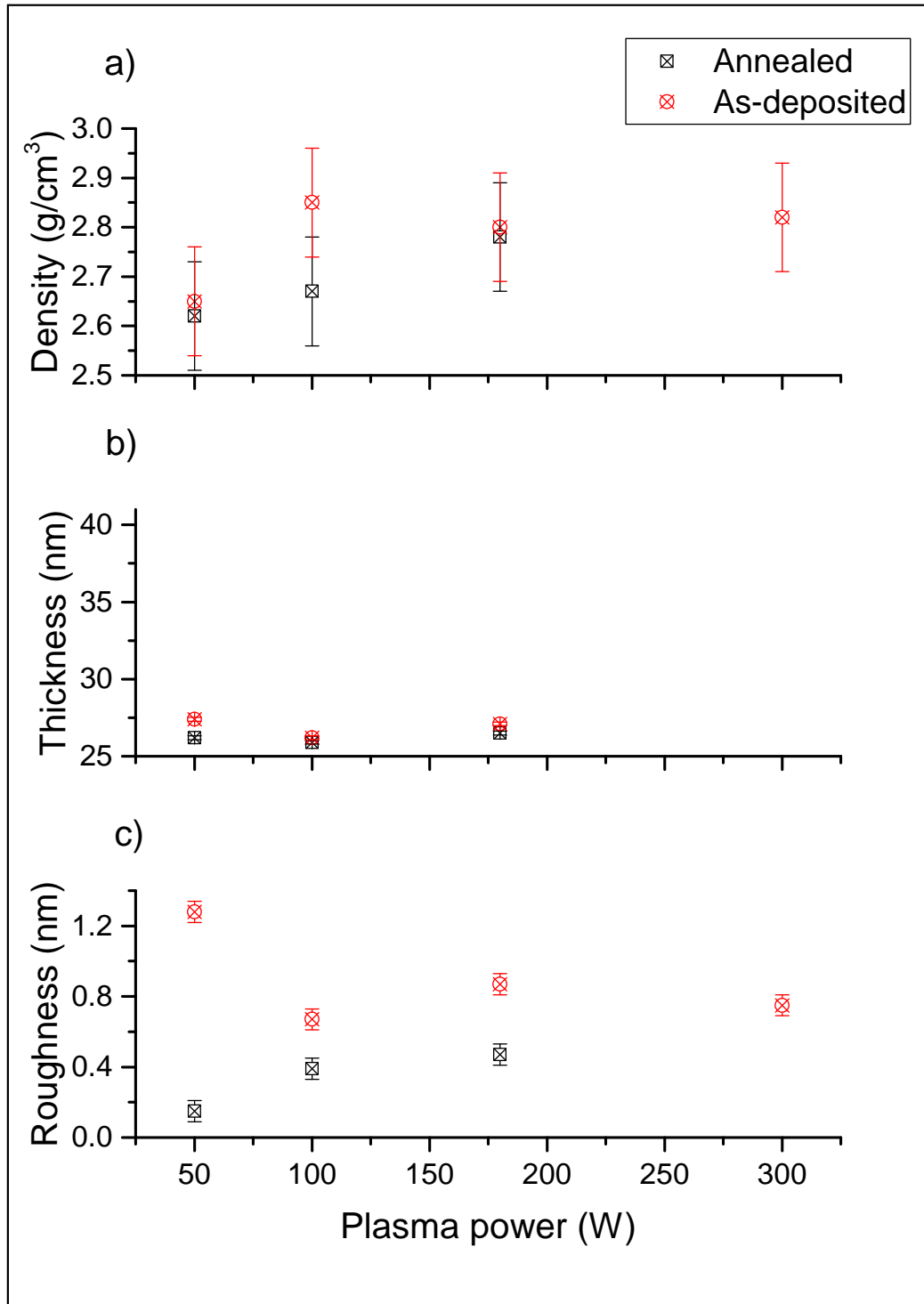
Figure 14. Density, thickness and roughness vs. plasma power for as-deposited and annealed Al_2O_3 samples. In density vs. plasma power dependence there is clear tendency of density growth with increasing plasma power if error margins of 0.11 g/cm^3 are included into consideration. 0.12 nm and 0.06 nm error margins were used for thickness and roughness, respectively, according to the formalized error. [31]

density increase of annealed and as-deposited samples consists 0.10-0.17 g/cm^3 with plasma power growth. The effect of the increased plasma power saturated the density improvement of as-deposited and annealed thin films starting from 100 W, where it was approximately 2.8 g/cm^3. In the case of annealing, a clear reduction of density could be observed on high plasma power values with respect to the as-deposited samples. This distinction was also prominent in the case of the reference thermal ALD samples which values were clearly higher than with the PEALD samples. This reduction of the density could be credited to an outgasing of impurities from the thin film due to the increased thermal activation. Besides density of the annealed samples is lower than as-deposited samples and it can be caused by restructuring of thin film during annealing.

According to the results for thickness, Figure 14 (b), the annealed and the as-deposited sample thicknesses have almost the same value and does not show any dependence on plasma power.

Also in Figure 14 (c) roughness data as a function of plasma power is represented. In case of the annealed samples, roughness increases with plasma power increase, while the as-deposited sample roughness fluctuates, but on the whole roughness of the annealed thin films is almost twice less than the as-deposited thin films. This corresponds with theoretical data stating that the surface of some materials smoothes when it is subjected to low-temperature annealing. Especially it is noticeable for 50 W plasma power where the highest roughness was produced and after annealing it reduced significantly. Other annealed and as-deposited samples produced at 100-300 W have similar roughness values. One of the reason of high surface roughness in PEALD process could be the very slight bombardment of plasma ions which causes its increase.

4.1.2 SiO$_2$

In this subsection, behaviour of thin film density, roughness and thickness with respect to plasma power, plasma time and thin film thickness is studied. The sample set had two different number of ALD cycles, SO1 means SiO$_2$ with 1000 cycles and SO3 means SiO$_2$ with 300 cycles. Thin film thicknesses of SO1 samples are more than 100 nm, while SO3 thin films have thickness less than 50 nm. The increased plasma power can influence thin film quality as high energy ions can damage thin film structure, however it can also lead to activation of the plasma gases more completely and therefore result to faster saturation and thus to reduced ALD cycle times.

The XRR measurements fitting results of SiO$_2$ samples found with XRR method are listed in Table 6. SiO$_2$ thickness, density and roughness relations to plasma power is represented in Figure 15. According to Figure 15 (a), as in case of Al$_2$O$_3$ there is no obvious dependence of thickness vs. plasma power and thickness values remain the same with plasma power increase. SO1 thicknesses are higher due to the more ALD cycles involved into the deposition.

According to the graph, Figure 15 (b), density dependence of SiO$_2$ samples shows slight decrease in case of SO3 samples and does not have significant increasing or decreasing trend in case of SO1 samples. SO1 samples stayed at the same value of about 2.10 g/cm^3 with respect to plasma power, while densities of SO3 samples dropped from 2.12 g/cm^3 to 2.05 g/cm^3. Overall change is lower than in case of Al$_2$O$_3$ and consisted less than 0.10 g/cm^3 that can be attributed to error margins. This could mean that there is small density dependence on the high plasma power SiO$_2$ process.

Table 6. XRR fitting results of SiO_2.

Sample identifier	Thickness, nm	Density, g/cm^3	Roughness, nm
SO1 1 s 50 W	148.00	2.09	0.36
SO1 1 s 180 W	147.00	2.10	0.19
SO1 3 s 180 W	137.80	2.12	0.35
SO1 6 s 180 W	121.10	2.21	0.26
SO1 1 s 300 W	147.00	2.10	0.54
SO3 1 s 50 W	45.20	2.12	0.33
SO3 1 s 180 W	45.40	2.06	0.49
SO3 3 s 180 W	41.30	2.10	0.45
SO3 6 s 180 W	37.10	2.23	0.27
SO3 1 s 300 W	45.80	2.05	0.73

Roughness analysis, Figure 15 (c), shows that number of cycles and plasma power influence it. The thicker the thin film the less roughness is observed. The result for roughness vs. plasma power shows that in the case of SO1 samples roughness decreases from 0.36 nm to 0.26 nm with increasing plasma power, while for SO3 samples roughness increases from 0.33 nm to 0.73 nm. However, in both cases the highest plasma power corresponds with the highest roughness values, 0.54 nm for SO1 and 0.73 nm for SO3. On average from the found results, it can be said that the thicker SiO_2 thin films are smoother in nanoscale than the thinner ones.

In Figure 16, density dependence vs. plasma times for SO1 and SO3 samples is shown. In both cases density increases with increasing plasma time which could be result of more complete and stoichiometric surface reactions due to the longer plasma gas flux to the surface. In addition, no statistically significant difference between thicknesses of the samples was shown.
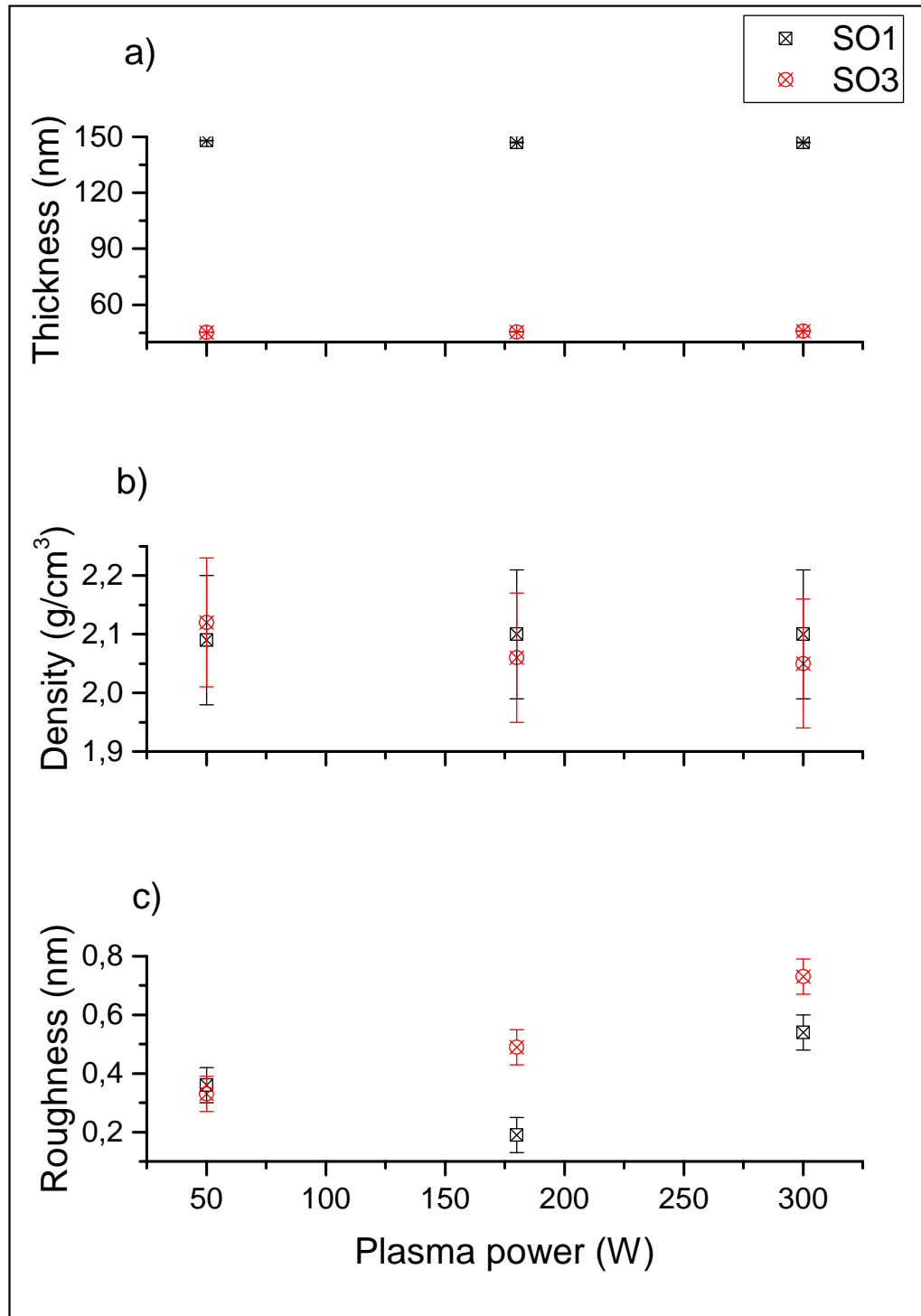
Figure 15. Density, roughness and thickness vs. plasma power for SiO_2 samples. 1000 cycles were used for SO1 samples and 300 cycles were used for SO3 samples. Plasma power values were the same for two types of samples. The error margins such as 0.12 nm for thickness, 0.11 g/cm^3 for density and 0.06 nm for roughness were used according to the formalized error. [31]
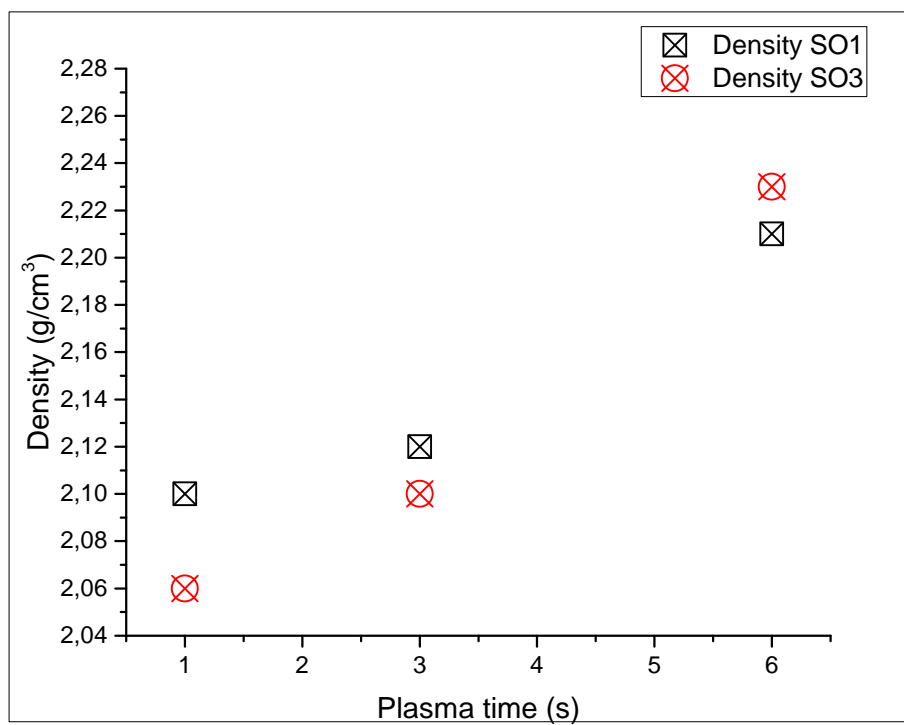
Figure 16. Density vs. plasma time for SiO_2 samples. 1000 cycles were used for SO1 samples and 300 cycles were used for SO3 samples. Plasma power value was 180 W for SO1 and SO3 samples.

4.2 ATR-FTIR measurement results

This section contains two separate parts including ATR-FTIR spectra results and analysis of Al_2O_3 and SiO_2 samples. Annealed Al_2O_3 analysis had to be neglected due to instrumental problems.

4.2.1 As-deposited Al_2O_3

ATR-FTIR spectra were studied to get information about different molecular bonds of the thin films. Such analysis helps understand if the deposited thin film is free from unwanted substances and consists only from the desired molecules. Figure 17 shows ATR-FTIR spectra of Al_2O_3 thin films in the transmission mode. Valleys in the graph identify molecular bonds of Al_2O_3. AO T Ref sample was produced with thermal ALD.

As a main result of ATR-FTIR spectra analysis of Al_2O_3 it is evident that there are no significant differences among the different plasma power, or with the thermal reference, samples. In Figure 17 in the range of 500-900 cm^{-1} there are several valleys that corresponds with the vibrations of Al-O bonds, where valleys at 570, 740 and 889 cm^{-1} are assigned as stretching modes and valley at 609 cm^{-1} is connected with the Al-O bending mode. [32, 33] Also the band around 609-611 cm^{-1} can be partially caused from Si-H vibration. [34] The bands between 1650-2700 cm^{-1} were excluded from the spectra because of systematic interference, most probably, due to the ATR crystal material. Sharp valley at about 1100-1105 cm^{-1} is associated with the Si-O stretching vibrations and the band at 818 cm^{-1} could be also connected to Si-O bending mode and it could be caused by native oxide or diffusion of oxygen into the substrate. [35, 36, 37] In the end of spectrum there is wide peak at 3550-3722 cm^{-1} that corresponds to O-H stretching mode which can be seen as an evidence of partially incomplete ALD cycles. [32, 33] The spectrum of 50 W Al_2O_3 sample having a pronounced -OH mode supports this data. There are also modes around 1300 and

1450 cm^{-1} referred to presence of CH$_3$, however there is no conclusive evidences to support that since some -CH3 vibration mode bands are missing from the spectra. [33] On the whole, the spectra of 100 W and 180 W samples correspond with the thermal ALD sample spectrum having the same level of incorporated impurities.
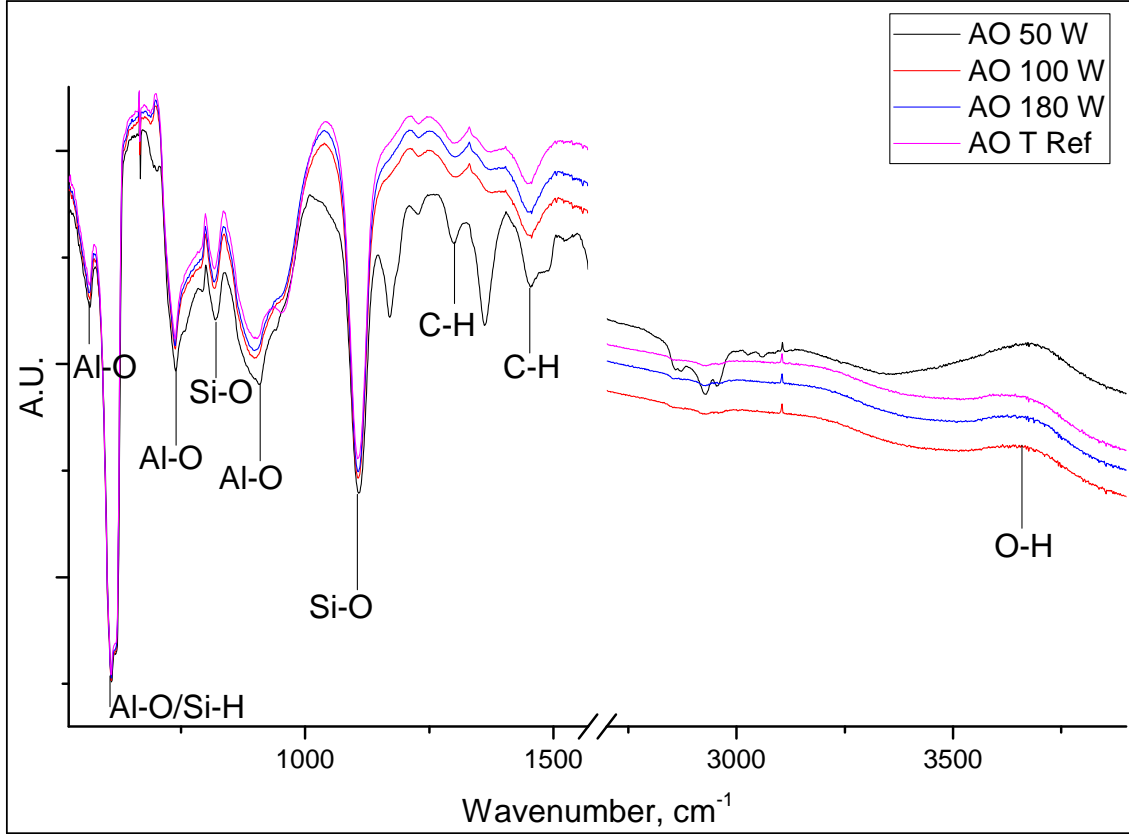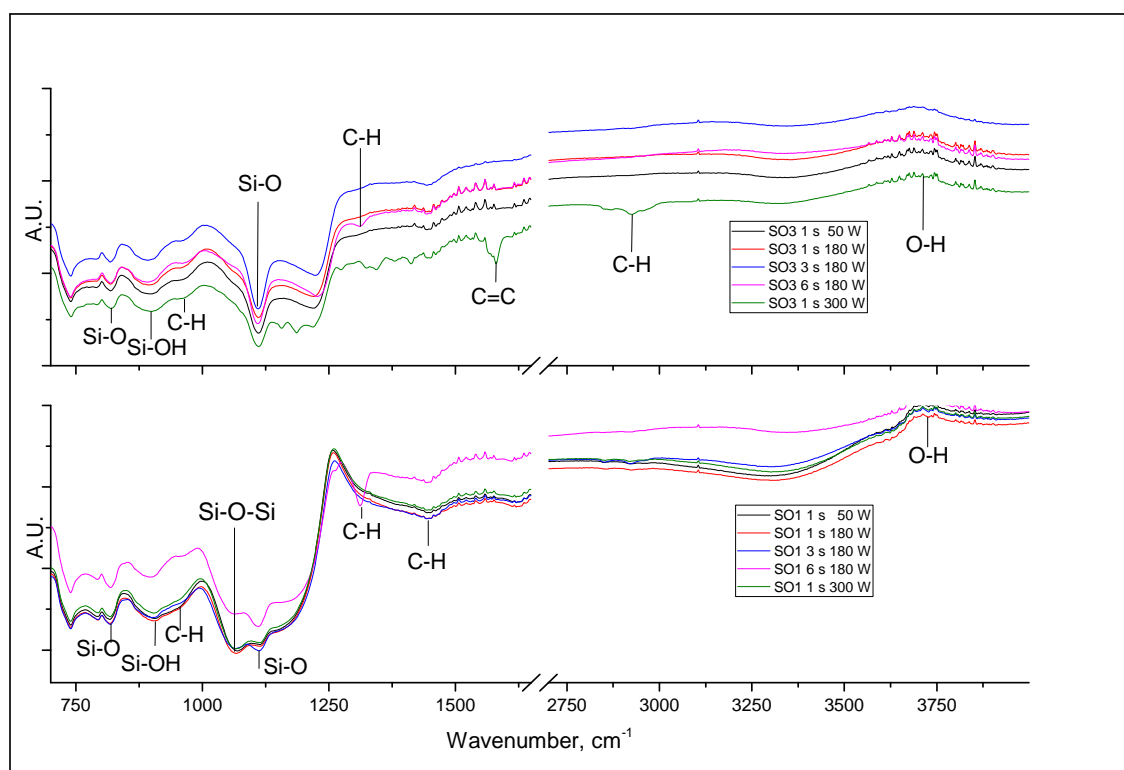

Figure 17. ATR-FTIR spectra of as-deposited ALD Al$_2$O$_3$ samples. Different plasma power and thermal reference FTIR results are presented to illustrate their effect on the thin film chemistry. The wavenumbers 1650-2700 cm^{-1} are excluded due to a systematic instrumental interference.

4.2.2 SiO$_2$

In Figure 18 ATR-FTIR spectra of SiO$_2$ samples is represented. The two graphs show similar spectra for SO1 and SO3, their comparable vibration band forms areas that hold qualitative information about the compounds of the samples. SO3 has a valley at 960 cm^{-1}, associated with CH$_3$ [38], that in case of SO1 it is a bit more

superimposed with 900 cm^{-1} valley band. However, in case of SO1 6 s 180 W sample it does not apply, probably, due to prolonged plasma time that removes CH$_3$ groups and can lead to improvement of SiO$_2$ thin film quality. Besides there is a valley at 1450 cm^{-1} that is also referred to CH$_3$. [39] In SO3 1 s 300 W there are 2800-3000 cm^{-1} stretching vibrations of CH$_3$, thus most probably these modes are observed due to CH$_3$ impurities. On the other SO3 samples this valley is not observed and, therefore, there is no certainty in the presence of CH$_3$ impurities. In case of SO1 samples there is a very minor band formed at 2800-3000 cm^{-1} except SO1 6 s 180 W. Thus, the thicker thin films seem to have detectable traces of CH$_3$ with larger certainty than the thin ones.

The broad band on two graphs at about 3600 - 3750 cm^{-1} is connected with the O-H stretch of the SiO-H. [38] These might be caused by incomplete ALD cycles and it apparently has an effect on the density values. Valley at 820 cm^{-1} is associated Si-O bending, while valleys at about 900 cm^{-1} and 1060 cm^{-1} are observed due to the stretching of Si-OH and Si-O-Si, respectively. [39, 40] SO3 1 s 300 W sample has a prominent valley at 1580 cm^{-1} that could be referred to double carbon stretching mode. [41] Besides two samples produced at 6 s 180 W have a valley at 1315 cm^{-1} that could be attributed to C-H bending mode. [41] It could be possible to conclude that high plasma process incorporates impurities in thin films but, however, no evident prove about presence of C=C and C-H modes in SiO$_2$ thin film was found.

Figure 18. ATR-FTIR spectra of SO1 and SO3 SiO$_2$ samples. SO1 samples were produced with 1000 ALD cycles, while SO3 samples were produced with 300 ALD cycles. Different plasma power results are presented to illustrate their effect on the thin film chemistry. The wavenumbers 1650-2700 cm^{-1} are excluded due to a systematic instrumental interference.

5 Summary

In this thesis, two plasma enhanced atomic layer deposition oxide thin films were studied using XRR and FTIR methods. SiO_2 and Al_2O_3 thin films were studied due to their high technological significance and potential as materials which by using PEALD can be further improved. The main varied experimental process parameter for both material was plasma power at low ALD temperature. For Al_2O_3, also as-deposited vs. 400 ℃ annealed thin films differences were studied. In addition, the effect of plasma time and ALD cycle number to SiO_2 thin film properties was under keen interest. Using XRR technique, structural characterization of thin films was obtained, while IR spectra of ATR-FTIR spectroscopy was qualitatively used to determine the chemical constitution of the samples.

It was found that density increases with plasma power for both annealed and as-deposited Al_2O_3 while for SiO_2 there is no apparent dependence revealed as density have similar values for SiO_2 produced with 1000 and 300 ALD cycles and within the error margins. Analysis of roughness showed that it increases with plasma power for Al_2O_3 and SiO_2 samples with the thinner thickness. The roughness of thicker SiO_2 samples does not change significantly. Besides there was no dependence between plasma power and thicknesses of the samples found.

According to ATR-FTIR results the structure of Al_2O_3 includes stretching and bending modes of Al-O bonds and also have sharp valley of Si-O bond. It might show a presence of native oxide. In IR spectra of SiO_2 and Al_2O_3 all the samples have a band formed around 3700 cm^{-1} which can be attributed to a presence of O-H groups, revealing that the PEALD process incorporates bonded hydrogen as impurity. Moreover, most of the samples have clear bands which could be related to CH_3 impurities but the characteristic stretching vibrations around 2800-3000 cm^{-1} are missing. Therefore, no certainty about their presence can be confirmed here. In the thick SiO_2 ATR-FTIR spectra there are very weak bands proving that these

samples probably have CH_3 impurities.

Overall, the performed analysis gives understanding how plasma parameters influence SiO_2 and Al_2O_3 oxide thin film density, roughness, thickness and molecular constitution. Further studies could cover other type of plasmas and plasma reactors to get deeper understanding of the physics and chemistry behind PEALD processes for oxide thin films.

References

[1] Diaz, B., Harkonen, E., Swiatowska, J., Maurice, V., Seyeux, A., Marcus, P., Ritala, M., *Low-temperature atomic deposition of Al_2O_3 thin coatings for corrosion protection of steel: surface and electrochemical analysis.* Corrosion science, Vol. 53, Issue 6, 2168-2175, 2011.

[2] Krishna, M. G., Vinjanampati, M., Purkayastha, D. D., *Metal oxide thin films and nanostructures for self-cleaning applications: current status and future prospects.* The European physical journal applied physics, Vol. 62, No. 3, 2013.

[3] Raut, H. K., Ganesh, V. A., Nair, A. S., Ramakrishna S., *Anti-reflective coatings: a critical, in-depth review.* Energy and environmental science, Vol. 4, 3779-3804, 2011.

[4] George, S. M. *Atomic layer deposition: an overview.* Chemical Reviews, Vol. 110, No. 1., 111-131, 2010.

[5] Sim, L. C., Ramanan, S. R., Ismail, H., Seetharamu K., N., Goh T., J., *Thermal characterization of Al_2O_3 and ZnO reinforced silicone rubber as thermal pads for heat dissipation purpose.* Thermochimica Acta, Vol. 430, Issue 1-2, 155-165, 2005.

[6] Smart, L. E., Moore, E., A., *Solid state chemistry: an introduction.* CRC press, 2012.

[7] Rees, O. J., *Fourier transform infrared spectroscopy: developments, techniques and applications.* Nova science publishers, Inc., 2010.

[8] Dasgupta, N. P., Meng, X., Elam, W. J., Martinson A. B. F., *Atomic Layer Deposition of metal sulfide materials.* Accounts of chemical research, Vol. 48, 341-348, 2015.

[9] Perros, A. C. P., *Thermal and plasma-enhanced atomic layer deposition: the study of and employment in various nanotechnology applications.* PhD Thesis, Aalto university school of electrical engineering, 2015.

[10] Bent, S., Harris J., McGehee Michael *Inorganic nanocomposite solar cells by atomic layer deposition.* GCEP research symposium, Stanford university, Stanford, CA, 2007.

[11] Puurunen, R. L., *Surface chemistry of atomic layer deposition: a case study for the trimethylaluminum/water process.* Journal of applied physics, Vol. 97, 121301-01 - 121301-52, 2005.

[12] Niskanen, A., *Radical enhanced atomic layer deposition of metal and oxides.* Academic dissertation, the Faculty of Science of the University of Helsinki, 2006.

[13] Puurunen, R. L., *Growth per cycle in atomic layer deposition: a theoretical model.* Chemical vapor deposition Vol. 9, Issue 5, 249-257, 2003.

[14] Miikkulainen, V., Leskelä, M., Ritala, M., and Puurunen, R., L., *Crystallinity of inorganic films grown by atomic layer deposition: Overview and general trends.* Journal of applied physics, Vol. 113, 021301-1 - 021301-101, 2013.

[15] Potts, S. E., Kessels, W., M., M., *Energy-ehanced atomic layer deposition for more process and precursor versatility.* Coordination chemistry reviews, Vol. 257, 3254-3270, 2013.

[16] Leskela, M., Ritala, M., *Atomic layer deposition: from precursors to thin film structures.* Thin solid films, Vol. 409, 138-146, 2002.

[17] Profijt, H. B., Potts, S., E., van de Sanden, M., C., M., Kessels, W., M., M., *Plasma-assisted atomic layer deposition: basics, opportunities and challenges.* Journal of vacuum science and technology A: vacuum, surfaces and films, Vol. 29, Issue 5, 2011.

[18] Colombi, P., Agnihotri, D., K., Asadchikov, V., E., Bontempi, E., Bowen, D., K., Chang, C., H., Depero, L., E., Farnworth, M., Fujimoto, T., Gibaud, A., and others *Reproducibility in X-ray reflectometry: results from the first world-wide round-robin experiment.* Journal of Applied Crystallography, Vol. 41, 143-152, 2008.

[19] Chason, E., Mayer T., M., *Thin film and surface characterization by specular X-Ray reflectivity.* Critical reviews in solid state and materials sciences, Vol. 22, Issue 1, 1-67, 1997.

[20] Yasaka, M., *X-ray thin film measurement techniques. V. X-ray reflectivity measurement.* The Rigaku Journal, Vol. 26, Issue 2, 2010.

[21] Cullity, B., D., *Elements of X-ray diffraction.* Addison-wesley publishing company, Inc., 1956.

[22] Tiilikainen J., Tilli J., M., Bosund V., Sormunen J., Mattila M., Hakkarainen T., and Lipsanen H., *Genetic algorithm using independent component analysis in x-ray reflectivity curve fitting of periodic layer structures.*, Journal of Physics D: applied physics, Vol. 40, No. 19, 2007.

[23] Griffiths, P., R., de Haseth, J., A., *Fourier transform infrared spectrometry.* John Wiley and Sons, Inc., 2007.

[24] Saptari, V., *Fourier-Transform spectroscopy instrumentation engineering.* SPIE press book, 2003.

[25] Smith, B. C., *Fundamentals of fourier-transform infrared spectroscopy.* CRC Press Taylor and Francis Group, LLC, 2011.

[26] Anderson, R. J., Bendell D., J., Groundwater P., W., *Organic spectroscopic analysis.* The royal society of chemistry, 2004.

[27] Sanghera, J. S., Aggarwal I., D., *Infrared fiber optics.* CRC Press LLC, 1998.

[28] *X'Pert PRO user's guide.* Koninklijke philips electronics N.V., 2000

[29] Tiilikainen, J., *Novel genetic fitting algorithms and statistical error analysis methods for X-ray reflectivity analysis.* Doctoral dissertation, Department of micro ans nanosciences, Helsinki university of technology, 2008.

[30] Wang, Z., Zhang, R., J., Lu, H., L., Chen, X., Sun, Y., Zhang, Y., Wei Y., F., Xu J., P., Wang, S., Y., Zheng Y., X., Chen L., Y., *The impact of thickness and thermal annealing on refractive index for aluminum oxide thin films deposited by atomic layer deposition.* Nanoscale research letters, 2015.

[31] Tiilikainen J., Mattila M., Hakkarainen T., and Lipsanen H., *Novel method for error limit determination in x-ray reflectivity analysis.* Journal of physics D: applied physics, Vol. 41, No. 11, 2008.

[32] Reyes, M. J., Ramos, B., M., Islas, C. Z., Arriaga W., C., Quintero P., R., Jacome A., T., *Chemical and morphological characteristics of ALD Al_2O_3 thin-films surfaces after immersion in pH buffer solutions.* Journal of the electrochemical society, Vol. 160, Issue 10, B201-B206, 2013.

[33] Goldstein, D. N., McCormick, J. A., George S., M., *Al_2O_3 atomic layer deposition with trimethylaluminum and ozone studied by in situ transmission FTIR spectroscopy and quadrupole mass spectrometry.* Journal of physical chemistry C, Vol. 112, Issue 49, 19530-19539, 2008.

[34] Wei, J. H., Sun, M. S., Lee S., C., *A possible mechanism for improved light-induced degradation in deuterated amorphous-silicon alloy.* Applied physics letters, Vol. 71, No. 11, 1997.

[35] Carmona-Tellez, S., Guzman-Mandoza, J., Aguilar-Frutis, M., Alarcon-Flores, G., Garcia-Hipolito M., Canseco M., A., *Electrical, optical and structural*

characteristics of Al₂O₃ thin films prepared by pulsed ultrasonic sprayed pyrolysis. Journal of applied physics, Vol. 103, 034105-1 - 034105-7, 2008.

[36] Martinet, C., Devine, R., A., B., *Analysis of the vibrational mode spectra of amorphous SiO₂ films.* Journal of applied physics, Vol. 77, No. 9, 4343-4348, 1995.

[37] Deshmukh, S., C., Aydil, E., S., *Low-temperature plasma enhanced chemical vapor deposition of SiO₂.* Applied physics letters, Vol. 65, No. 25, 3185-3187, 1994.

[38] Deshmukh, S., C., Aydil, E. S., *Low-temperature plasma enhanced chemical vapor deposition of SiO₂.* Applied physics letters, Vol. 65, Issue 25, 1994.

[39] Burton, B. B., Kang, S. W., Rhee, S. W., George S. M., *SiO₂ atomic layer deposition using tris(dimethylamino)silane and hydrogen peroxide studied by in situ transmission FTIR spectroscopy.* Journal of physical chemistry, Vol. 113, Issue 19, 8249-8257, 2009.

[40] Shokri, B., Firouzjah, M. A., Hosseini S., I., *FTIR analysis of silicon dioxide thin film deposited by metal organic-based PECVD.* Proceedings of 19th international symposium on plasma chemistry society, Bochum, Germany, 2009.

[41] Coates, J., *Interpretation of infrared spectra, a practical approach.* Encyclopedia of analytical chemistry, 10815-10837, John Wiley and Sons Ltd., Chichester, 2000.